

## Investigation of intrinsic defects in core-shell structured ZnO nanocrystals

S. K. S. Parashar, B. S. Murty, S. Repp, S. Weber, and E. Erdem

Citation: *Journal of Applied Physics* **111**, 113712 (2012); doi: 10.1063/1.4725478

View online: <http://dx.doi.org/10.1063/1.4725478>

View Table of Contents: <http://scitation.aip.org/content/aip/journal/jap/111/11?ver=pdfcov>

Published by the [AIP Publishing](#)

---

### Articles you may be interested in

[Bicolor Mn-doped CuInS<sub>2</sub>/ZnS core/shell nanocrystals for white light-emitting diode with high color rendering index](#)

*J. Appl. Phys.* **116**, 094303 (2014); 10.1063/1.4894246

[Defect-induced ferromagnetism in ZnO nanoparticles prepared by mechanical milling](#)

*Appl. Phys. Lett.* **102**, 072408 (2013); 10.1063/1.4793428

[High temperature ferromagnetism and optical properties of Co doped ZnO nanoparticles](#)

*J. Appl. Phys.* **108**, 084322 (2010); 10.1063/1.3500380

[Relationship between oxygen defects and the photoluminescence property of ZnO nanoparticles: A spectroscopic view](#)

*J. Appl. Phys.* **106**, 094314 (2009); 10.1063/1.3256000

[Correlation between microstructure and optical properties of ZnO nanoparticles synthesized by ball milling](#)

*J. Appl. Phys.* **102**, 093515 (2007); 10.1063/1.2804012

---



## Investigation of intrinsic defects in core-shell structured ZnO nanocrystals

S. K. S. Parashar,<sup>1</sup> B. S. Murty,<sup>2</sup> S. Repp,<sup>3</sup> S. Weber,<sup>3</sup> and E. Erdem<sup>3,a)</sup>

<sup>1</sup>*School of Applied Sciences, Kalina Institute of Industrial Technology, KIIT University, Bhubaneswar 751024, India*

<sup>2</sup>*Department of Metallurgical and Materials Engineering, Indian Institute of Technology Madras, Chennai 600036, India*

<sup>3</sup>*Institut für Physikalische Chemie, Universität Freiburg, Albertstraße 21, 79104 Freiburg, Germany*

(Received 29 December 2011; accepted 7 May 2012; published online 8 June 2012)

Nanocrystalline ZnO particles were prepared using the high-energy ball milling technique and investigated with electron paramagnetic resonance (EPR), impedance, and Raman spectroscopy to reveal the origin of surface and core defects. We observed two distinct EPR signals with different  $g$ -factors,  $g \sim 2.0$  and  $\sim 1.96$ , indicating EPR-active defects on the surface and core, respectively. Using the semi-empirical *core-shell* model, we identified that sufficiently small nanocrystals (below 30 nm) can show p-type character. The model can also explain the origin of the non-linearity of the  $U$ - $I$  behaviour in nanocrystalline ZnO. © 2012 American Institute of Physics. [<http://dx.doi.org/10.1063/1.4725478>]

### I. INTRODUCTION

Intrinsic and extrinsic defects in bulk and nano-sized ZnO materials have been investigated intensely for quite some time both experimentally and theoretically, and the results have been summarized in excellent monographs and reviews.<sup>1-3</sup> The microscopic origin of such defects is, however, still under debate. This is due to the lack of microscopic investigations, which yield direct information on the electronic structure and the environment of defect centres. Standard bulk characterization techniques are not well suited for the analysis of such defect centres. Electron paramagnetic resonance (EPR) spectroscopy, however, is one method of choice, which affords, due to its extensive selectivity and sensitivity towards centres with unpaired electrons, examination of defects, and their environment even at very low concentrations. Although a wealth of papers on ZnO is found in the literature, the role of defects in nanoscale-structured defect chemistry, preparation technique, and defect properties have not received much attention to date. Despite its simple chemical formula, ZnO has a very rich defect chemistry.<sup>4</sup> It is well known that the ZnO structure is relatively open with a hexagonal close-packed lattice, where the Zn atoms occupy half of the tetrahedral sites. All the octahedral sites are empty, hence, there are plenty of sites in ZnO to accommodate intrinsic defects and extrinsic dopants.<sup>5</sup> These defect-related issues are of particular interest for ZnO, which is an important semiconductor with widespread applications.<sup>6,7</sup> With respect to the abundance of surface morphologies, ZnO offers the most diverse nanostructures of any material known today. Its large direct band gap of 3.437 eV and the large exciton binding energy of  $E_B = 60$  meV at room temperature make ZnO a prominent candidate for device applications. The key challenge that needs to be overcome for practical realization of most ZnO-based applications is the fabrication of p-type

material. P-type ZnO may be obtained by doping<sup>5</sup> of group-I elements on Zn-sites or group-V elements on O-sites. Although significant progress has been made recently,<sup>8</sup> full control over the materials' conductivity type has still to be achieved. Hence, comprehensive investigations of the fundamental properties of acceptors in ZnO and the study of surface defects on a nanoscale are needed.<sup>9</sup> Here, we demonstrate clearly how n-type ZnO can be transformed into p-type ZnO without doping. Such transformation of n-type ZnO nanocrystals could in principle offer a new approach to using p-type ZnO semiconductors in device technology.

Intrinsic defects play a vital role for changing the properties of nanocrystals. For a deeper understanding of the intrinsic and extrinsic defects in undoped and doped nanocrystalline ZnO, further improving synthetic control and dopant incorporation, optimisation of their concentrations and processing, and investigations of emerging phenomena are required. Defect studies have been considered for more than 50 years, but now there is need for a revisit in the context of normal applications using nanostructured materials. In the past, defect chemistry was studied in relation to ZnO properties and applications as ZnO varistor: defects significantly alter the grain boundary (GB) properties and also  $U$ - $I$  characteristics. But the origin of non-linearity in  $U$ - $I$  characteristics in nanoscale ZnO is still not clear.

Just from the basic principles of defect formation, it is far from being straightforward to determine which types of intrinsic defects could be present in the sample. The origin of these defects and their assignment are still controversial issues. Conceivably, probable intrinsic defect centers in ZnO are: (i) zinc vacancies ( $V_{Zn}$ ), (ii) zinc on interstitial sites ( $Zn_i$ ), (iii) oxygen on interstitial sites ( $O_i$ ), and (iv) oxygen vacancies ( $V_O$ ). From the perspective of EPR, these four probable intrinsic defects can be rationalized as follows: (i) The EPR signal from  $V_{Zn}$  defect centers should have a  $g$ -factor larger than the one of the free electron,  $g \geq 2.0023$  (Ref. 10) when a hole is involved as lattice defect.<sup>11</sup> (ii) Observation of  $Zn_i$  defect centers by EPR is not possible.  $Zn_i$  as an interstitial has an electronic

<sup>a)</sup>Author to whom correspondence should be addressed. Electronic mail: [emre.erdem@physchem.uni-freiburg.de](mailto:emre.erdem@physchem.uni-freiburg.de).

configuration ending with  $4s^2$ , and thus, is diamagnetic. There must be an external effect, such as light or thermal, to transfer an electron into the conduction band of ZnO ( $Zn_i^+ + e$ ). The EPR signal of a paramagnetic  $Zn_i^+$  state can only be detected when the electronic wave functions of  $Zn_i^+$  centres do not overlap so that a metastable impurity level arises where the unpaired  $4s^1$  electrons are localized and detectable by EPR.

(iii) Oxygen on interstitial sites ( $O_i$ ) has possible electronic configurations ending with  $2p^4$ ,  $2p^5$ , and  $2p^6$ , giving  $O_i$ ,  $O_i^-$ , and  $O_i^{2-}$ , respectively. The  $O_i^{2-}$  state is diamagnetic, and therefore, EPR inactive. The  $O_i$  state with the  $2p^4$  configuration has a triplet multiplicity. The  $O_i^-$  state with the  $2p^5$  electronic configuration can be attributed as paramagnetic centre which can be easily observed by EPR. However, the interaction of paramagnetic defects with other diamagnetic or paramagnetic defects of ZnO for this centre has to be taken into account.<sup>12</sup>

(iv) Oxygen vacancies can be recognized in three possible states: (a) A diamagnetic oxygen vacancy that does not trap an electron with respect to the lattice. This vacancy is doubly positively charged and can be safely assigned as  $V_O^{2+}$ . It has four surrounding  $Zn^{2+}$  ions so that it is rendered diamagnetic because there are no unpaired electrons left. (b) The vacancy of oxygen occupied by an electron assigned as  $V_O^+$ . This vacancy originates by reduction, trapping an electron from the conduction band so that, with respect to the lattice, it carries one positive charge. This defect centre may also be assigned as a F-centre in alkali halides. (c) Finally, the vacancy attributed as  $V_O$  is neutral compared to the lattice and captures two electrons. The  $V_O$  defect centre is diamagnetic when the spins of both electrons captured in the vacancy somehow compensate. If they do not, then one may expect the existence of a triplet state, which is also an EPR-active center.

Different techniques are routinely utilized to produce ZnO nanocrystalline materials, such as sol-gel,<sup>8</sup> hydrothermal,<sup>13</sup> solution-based,<sup>14</sup> and combustion<sup>15</sup> methods, and many more.<sup>16</sup> All these chemical and metallo-organic methods have drawbacks with respect to large-scale production, reproducibility, maintenance of stoichiometry, and homogeneity in composition, and furthermore, require external high calcination temperatures<sup>17</sup> of 350 °C and above for the processing of mono-phases. In contrast to the above-mentioned techniques, high-energy ball milling (HEBM) provides an environmentally friendly way to prepare ZnO nanoparticles with exceptionally high diffusivity, sinterability, and unusual formability in conventionally brittle materials at room temperature.<sup>18</sup>

In this contribution, we propose a *core-shell* model to explain intrinsic defects in nanostructured ZnO. A new mechanism is revealed by which the intrinsic defects arising in nanostructured ZnO can be understood. This will help to tailor specific properties of nanostructured materials for nano-device applications such as field-effect transistor (FET)<sup>19</sup> thin film printing,<sup>20</sup> and many others based on nano-architectures such as nanorods,<sup>21</sup> nanowires,<sup>1</sup> or nanocables.<sup>22</sup>

## II. EXPERIMENTAL

We have used x-ray diffraction, EPR, Raman, and impedance spectroscopy methods to characterize ZnO

nanocrystalline materials. Details of each characterisation method, experimental conditions, and the synthesis route of the materials are given in the supplementary information.<sup>61</sup>

## III. RESULTS AND DISCUSSION

The average crystallite size of the ZnO was determined from x-ray peak (101) broadening using a Voigt peak profile analysis after eliminating the instrumental broadening and strain contributions. It was observed that the crystallite size decreases with increasing milling time as shown in Fig. 1(c) of the supplementary information.<sup>61</sup> Specifically, the nanocrystallite size of ZnO ranges from 200  $\mu\text{m}$  before milling to 22 nm after 7 h of milling.

To learn more on intrinsic defects in ZnO, we used X-band and Q-band EPR by which one can not only determine the concentration of paramagnetic defect centres but also obtain detailed information on the electronic and structural properties of defects in their nanocrystalline surroundings. In Fig. 1, we present results from continuous-wave EPR at (a) X-band and (b) Q-band obtained at room temperature. In the X-band data, we identify two groups of signals that can be assigned to different defect centres, one around  $g \sim 1.96$  and the other around  $g \sim 2.00$ . These two signals have been often reported, either showing up isolated<sup>23,24</sup> or both simultaneously,<sup>19,20,25</sup> however, their assignment is still controversially discussed.<sup>9,10,12,24–36</sup> Recently, by means of optically detected magnetic resonance,<sup>37–39</sup> both zinc and oxygen vacancies have been detected. Below we will give an overview on the different viewpoints in assigning these two EPR signals.

The precise origin of the signal with a  $g$ -factor around 1.96 is still not fully established. This signal is generally attributed to a shallow donor and assigned to the presence of singly ionized oxygen vacancy defects ( $V_O^+$ ).<sup>25,40–42</sup> However, in some cases, it was also attributed to unpaired electrons trapped on oxygen vacancies<sup>41</sup> or shallow donor centers such as ionized impurity atoms in the crystal lattice of ZnO.<sup>29,32,43</sup> Even an assignment to free carriers in the conduction band has been put forward.<sup>33</sup> In contrast to these assignments, there are reports supposing that the EPR signal at  $g \sim 1.96$  may be due to one electron being weakly bound to ionized impurity atoms.<sup>44</sup> This would mean that the electron from a shallow donor level is not completely delocalized into the conduction band but stays weakly bound to the original atoms, and behaves much like an electron in a hydrogen-like atom with a large Bohr radius.<sup>44</sup> Irradiation with UV-light is expected to produce excitations and, once bound, this excitation would give rise to a paramagnetic signal at  $g \sim 1.96$ , thus, suggesting that the signal is not related to oxygen vacancies.<sup>44</sup> Furthermore, arguments in favor of a Zn-O divacancy or even a Zn-O-Zn trivacancy have been presented for the origin of this center.<sup>45</sup> Recently, this center was used for monitoring electron photoexcitation from the deep level centres in ZnO gap<sup>46</sup> or photoexcitation of the conducting electrons from Pb centers<sup>37</sup> where they related this photosensitive defect centre to conduction electrons located at donor centers in *bulk* and near the surface of ZnO particles. The photosensitive nature of this signal, i.e., its

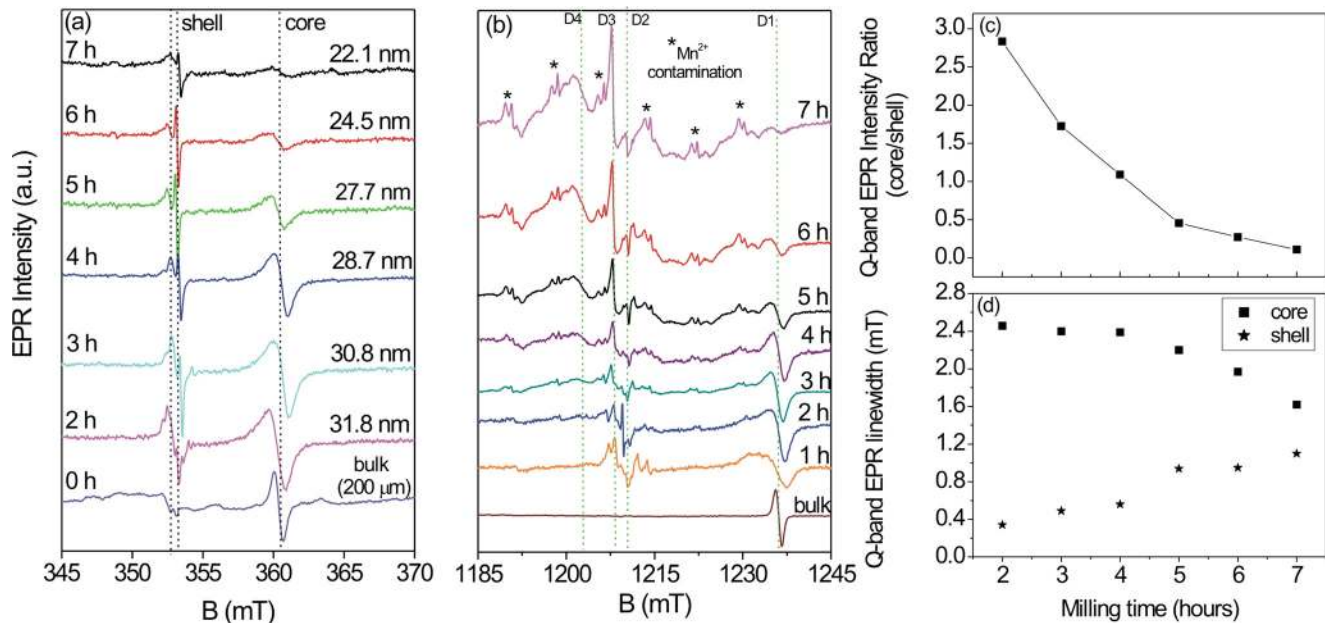


FIG. 1. Room temperature EPR spectra of ZnO nanocrystals measured by (a) X-band and (b) Q-band microwave frequencies. Signals from  $\text{Mn}^{2+}$  impurities are marked with asterisks. (c) The ratio of the *core* (D1) and the *shell* (D3) signal deduced from Q-band EPR spectra as a function of the milling time. (d) The linewidths of the Q-band EPR signals (peak-to-peak) arising from the D3 surface defect centre and the D1 bulk defect centre. Milled 0.5 h and 1 h samples were not included since their EPR signals were not sufficiently resolved so that intensity and linewidth parameters could not be unambiguously extracted.

enhancement in UV-light,<sup>20</sup> supports that this signal could also be attributed to electrons in conduction-band states, since UV-light can promote electrons into these sites.<sup>47</sup> In case of extrinsic  $\text{Co}^{2+}$  doping,<sup>48</sup> the signal at  $g \sim 1.96$  was not observed due to broadening by fast spin-spin relaxation of the shallow donor electrons in the presence of the many unpaired Co *d*-electrons. The same effect holds for Mn and Fe doping (extrinsic defects). Recent theoretical studies<sup>12,26</sup> reported first-principles calculations showing that the oxygen vacancy mainly assigned for the  $g \sim 1.96$  signal is not a shallow donor but a deep donor. Thus, oxygen vacancies are not responsible for the n-type conductivity often observed in ZnO.<sup>12,26</sup>

EPR investigations on undoped ZnO have been presented before,<sup>24,28,31,49–51</sup> and the signal at around  $g \sim 2$  has been assigned to a singly ionized Zn vacancy in Refs. 28 and 50, whereas others have attributed this signal to an unpaired electron trapped in an oxygen vacancy site,<sup>24,49,51</sup> i.e.,  $\text{F}^+$  center.<sup>31</sup> The former assignment is based on the resolved hyperfine interactions with the four neighboring Zn nuclei, which has only been seen when ZnO was irradiated.<sup>35</sup> This is consistent with the results from density functional theory calculations<sup>26</sup> which indicate that a certain excitation is required to generate the paramagnetic +1 state. On the other hand, the  $\text{O}^{2-}$  ion vacancies at the ZnO surfaces<sup>30</sup> are stable and can trap electrons under interaction of external magnetic field to form paramagnetic centers (F-centers), and generate a stable EPR signal at  $g \sim 2.0$  originating from  $\text{O}^{2-}$  vacancies. In summarizing, we shall note that considerable conflicts in the assignment of the EPR signals near  $g \sim 1.96$  and  $g \sim 2.0$  persist.

Recently, we have proposed a *core-shell* model in the framework of quantum-size effects<sup>52</sup> to describe the two centres in ZnO ultrafine nanoparticles. In this model, the

EPR signal at  $g \sim 1.96$  originates from defects in the bulk (*core*), whereas the signal near  $g \sim 2.00$  arises from surface defects (*shell*). Closer inspection of the X-band EPR spectrum near  $g \sim 2.00$  reveals a separation into two EPR lines when going from the bulk to nano-size dimensions. EPR of bulk ZnO shows one signal from both surface defects (*shell*) and *core* at  $g \sim 2.00$  and  $g \sim 1.96$ , respectively. Here, it is worthy to note that, right after the HEBM process (from bulk to 2 h milling) both defect signals revealed significantly increased EPR intensity and asymmetric line-shape broadening. This is an expected effect due to mechanical activation of defect centres both at the surface and the *core* during milling. Additional milling (performed in this study up to 7 h) leads to further decreasing crystallite sizes, and accordingly, to a decreasing *core* signal amplitude and an increasing *shell* signal amplitude. The same trends have been observed in the Q-band EPR spectra (Fig. 1(b)). Additionally, by Q-band EPR, three different surface defect centres indicated as D2, D3, and D4 are resolved (see Fig. 1(b)) with  $g$ -values of  $g_{\text{D2}} = 2.004$ ,  $g_{\text{D3}} = 2.010$ , and  $g_{\text{D4}} = 2.012$ . Given the above-mentioned ambiguities in signal assignments, we refrain here from further speculations and refer the reader to work by Kakazey *et al.*<sup>31</sup> who have attempted a signal attribution. But clearly, additional studies are required to further substantiate their findings. Since Q-band EPR is quite sensitive, we observed also signals from  $\text{Mn}^{2+}$  impurities, which may originate from the preparation stage or arise from the starting materials.

The exact  $g$ -value of the *core* defect centre D1 deduced from Q-band EPR is  $g_{\text{D1}} = 1.964$ . From an analysis of signal intensities and line shapes, we obtained the particle-size-dependent *core*(D1)/*shell*(D3) ratio (Fig. 1(c)) and linewidths (Fig. 1(d)). Note that signals from surface defects, designated as D2 and D4, were not further analyzed since they were

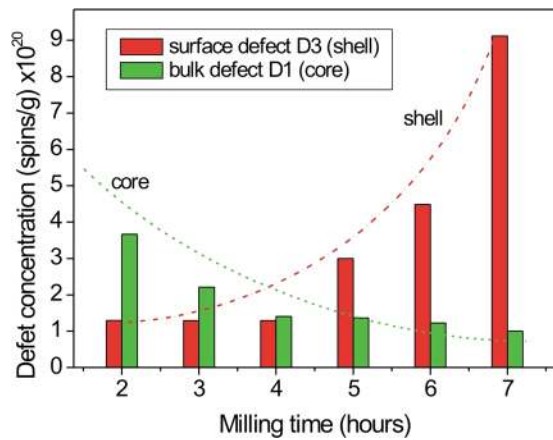


FIG. 2. Defect concentrations in the *core* and at the surface (*shell*) of differently sized ZnO nanocrystallites determined by the spin counting procedure.

not fully resolved even at Q-band microwave frequencies. To better resolve the D2 and D4 signals, it is necessary to examine the milled ZnO samples by EPR at very high microwave frequencies, e.g., by using W-band EPR or EPR at even higher frequencies. This, however, will be deferred to a subsequent publication. Fig. 1(c) clearly reveals strong size effects on reaching the nanoscale. This can be rationalized by applying the *core-shell* model to the ZnO nanoparticles. The theoretical foundations of the *core-shell* model have been published recently.<sup>19</sup> Using the *core/shell* ratio, we determined the thickness of the surface layer as 0.5 nm. This compares to a thickness of 1 nm for ZnO samples synthesized by microwave heating route.<sup>19</sup> This shows that the mechanical milling causes high strain on the particle surface, thus, leads to line broadening in the *shell* signal. We conclude that the crystallite-size dependent observed spectral changes in the X- and Q-band EPR spectra are directly related to the surface properties of these nanocrystals.

Using the spin-counting procedure, the concentration of defect centres can be determined from the EPR spectra; details can be found in the supplementary information.<sup>61</sup> Calculated by this method, the defect concentration dependence as a function of the milling time is shown in Fig. 2. The number of surface defects increases drastically with increasing milling time. After 7 h of milling, more than 8 times as

many surface defects were found than after 2 h. Simultaneously, the number of core defects decreased by a factor of 4 when going from 2 to 7 h of high-energy ball milling. These results agree well with the proposed *core-shell* model,<sup>19,52</sup> which we outline schematically in Fig. 3.

Crystalline ZnO (bulk) has a hexagonal Wurtzite structure of point-group  $P6_3mc$ . Nanocrystals are formed when the size of bulk crystalline ZnO decreases below 100 nm. A number of physical phenomena, such as quantum-size (quantum tunnelling) and surface effects (structural effects), emerge for nanocrystal sizes below 30 nm. In nanocrystalline ZnO, different intrinsic defects develop in the *core* (negatively charged defects), in the *shell* (positively charged defects), and at the GB. Surface defects become dominant in mechanically activated ZnO nanoparticles, whereas bulk defects prevail in non-mechanically activated ZnO.

Raman scattering is a sensitive method that yields information on crystal structure and structural defects (see supplementary Fig. 2).<sup>61</sup> A blue shift of the Raman peak observed when going to nanoscale suggests a possible donor-acceptor pair recombination or trapping of electrons inside ZnO nanocrystals.<sup>53,54</sup> This increases the charge density, and hence, the concentration of positively charged defects. Consequently, this will lead to increased Hall conductivity. Remarkably, when the *shell* is positively charged it may provide an opportunity to produce p-type semiconductivity by *core-shell* ZnO nanocrystals without any doping ion.

To examine the transport properties of nanocrystalline ZnO ceramic, we employed the two-point dc method for electrical measurements. Figs. 4(a)–4(c) show potential-versus-current ( $U$ - $I$ ) curves of differently milled ZnO samples. It is well known that contact properties depend on the work function between the electrodes and the semiconductor samples and also on the type of majority carriers. When the work function of the ceramic is smaller than that of the semiconductor material, the n-type semiconductor exhibits an ohmic contact, because the work function of ZnO is 5.30 eV.<sup>55,56</sup> A linear  $U$ - $I$  curve of the 2 h milled ZnO nanocrystal is shown in Fig. 4(a) indicating that this material is an n-type semiconductor being ohmic in nature.

In Figs. 4(b) and 4(c), three distinct regions can be recognized in the  $U$ - $I$  plots; in other words, three kinds of conductivity due to a specific mixture of charge carriers exist: a

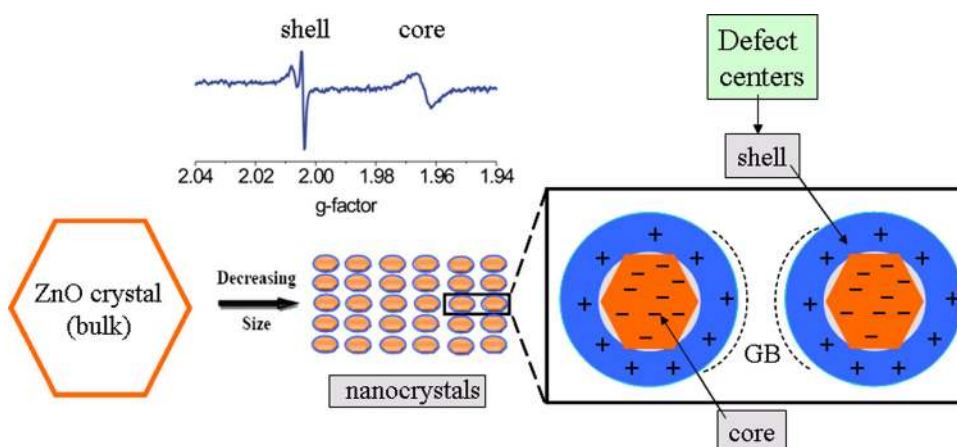


FIG. 3. Schematic representation of the *core-shell* model to rationalize intrinsic defects in nanocrystalline ZnO observed by EPR spectroscopy (GB: Grain boundary).

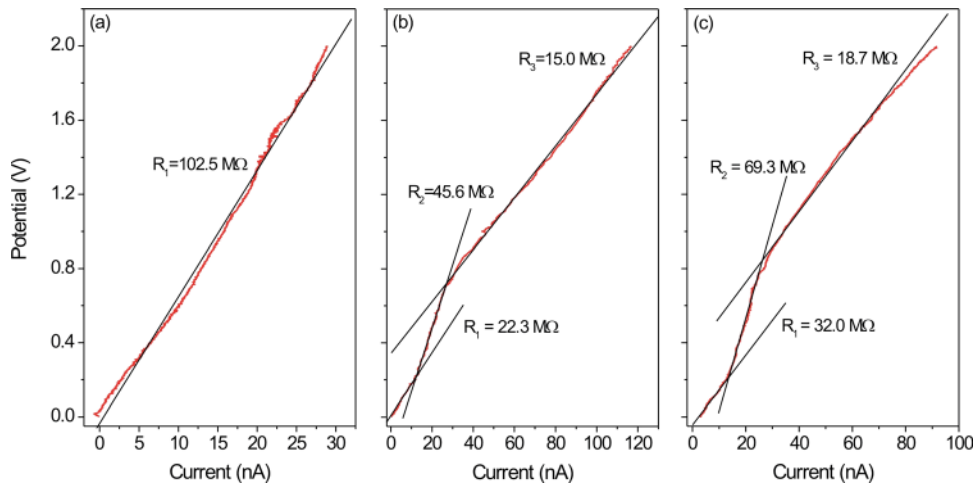


FIG. 4. Potential-versus-current ( $U$ - $I$ ) measurements at room temperature for (a) 2 h, (b) 4 h, and (c) 7 h milled ZnO samples.

leakage region (slow-conduction),  $R_1 = 22.3 \text{ M}\Omega$  and  $R_1 = 32.0 \text{ M}\Omega$ , a voltage clamping region (conduction),  $45.6 \text{ M}\Omega$  and  $69.3 \text{ M}\Omega$ , and an upturn region (saturation),  $15.0 \text{ M}\Omega$  and  $18.7 \text{ M}\Omega$ , with the specified values for 4 h and 7 h milled ZnO samples, respectively. In the leakage region, the resistance of the 2 h nanocrystalline ZnO sample is  $102.5 \text{ M}\Omega$ , which is larger than that of the 4 h and 7 h milled samples. There are several theoretical as well as experimental reports for the non-linearity in the  $U$ - $I$  characteristics of the bulk sample.<sup>55,57</sup> However, none of the theories presented in these reports are able to explain the origin of non-linearity in the nanocrystalline materials. However, the mechanisms responsible for this type of behaviour in all nanostructured materials examined here can be described by the proposed *core-shell* model (Fig. 3). By this model, the defect-charge density of nanocrystalline ZnO is divided into two parts at equilibrium, with a contribution from the inner *core* (linear) and one of the outer *shell* (non-linear). One or more of the following reasons may be responsible for the non-linearity in nanostructured ZnO materials:

- (i) Defect distribution and interactions in the surface structure, i.e., surface polarization, atomic termination, quantum tunnelling, interactions of *shell-shell*, *core-core*, *core-shell*, GB-GB, *shell-GB*, *core-GB*, interaction or absorption of trapped defect centres within the *core-shell* of the nanostructured materials (see Fig. 3).
- (ii) Decrease of the *core* size with respect to the *shell* size of ZnO nanocrystals with increasing milling time (see Figs. 2, 3, and 5).
- (iii) Different kinds of size distributions may be present in the sample which is the source of the trapped and surface defects causing clamping or creating an easy path for conduction of the current. Thus, such kind of intrinsic process affects the linearity of the  $U$ - $I$  behaviour and causes non-linearity (see Fig. 4).

It is also observed that the GB plays a vital role to control the electrical properties of nanocrystalline ZnO.<sup>58,59</sup> However, when the *core* size of ZnO decreases to less than the *shell* size, i.e., the defect density increases (Fig. 2) on the surface of the core, hence increased non-linearity was observed in Figs. 4(b) and 4(c). A quasi-periodic variation in the conduction and valence band throughout the microstructure may occur. Thus, in nanocrystalline ZnO, where the crystallite size is less than 30 nm, the nature of the conduction process may be different and quantum-size effects become dominant.

The electrical properties of differently milled nanocrystalline ZnO ceramic samples were measured and are shown in supplementary Fig. 3.<sup>61</sup> The specific resistivity is reduced drastically with increasing milling time. The relatively low resistivity demonstrates that high carrier concentrations can also be generated during longer periods of milling. This also indicates the increase of the electrical conductivity by a factor of 3.5 when decreasing the crystallite size.

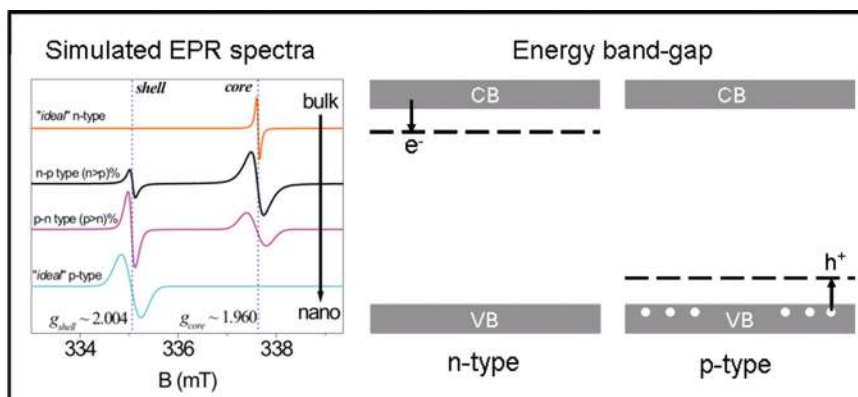


FIG. 5. Schematic representation of simulated EPR spectra and the energy band gap of n-type and p-type ZnO nanocrystallites.

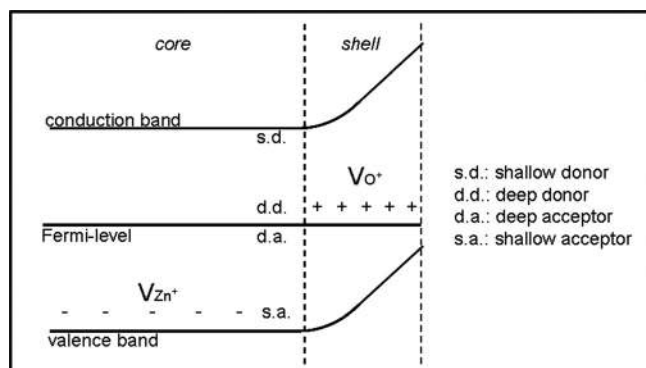


FIG. 6. Schematic illustration of the band gap as a function of the defect structure in *core-shell* structured nano-sized ZnO. It shows that the oxygen vacancies at the surface are deep donors and the Zn vacancies on the *core* are shallow acceptors.

According to our EPR and resistivity data as well as from a rationalization with the *core-shell* model, we present schematically an overview of the relation between crystallite size, EPR  $g$ -factor shift, and the electronic behaviour of ZnO materials in Fig. 5. The reduction of ZnO to nanosize leads to p-type semiconductivity through the formation of a surface defect complex that increases the number of holes relative to the number of free electrons (Figs. 3 and 5). This *core-shell* model is in very good agreement with our experimental findings and simulated data (Fig. 5), and opens a new direction of research to understand the intrinsic defect mechanism in nanostructured materials and the nonlinearity in  $U$ - $I$  characteristics.

In Fig. 6, we present a schematic illustration of our defect assignment. The *core* is dominated primarily by shallow acceptors, whereas at the *shell* deep donors prevail. As a consequence, the development of p-type ZnO is favorable for sufficiently small particle sizes (below 30 nm). The *core-shell* model suggests the negative charging of the *core* and positive charging of the *shell*. This is supported by the decrease in EPR intensity of the signal at  $g \sim 1.96$  upon decreasing the crystal (*core*) size. Clearly, more oxygen vacancies are formed on the surface than in the *core*, and conversely, more Zn vacancies are formed on the *core* than in the *shell*.

Independent from our *core-shell* model, by a recent examination of Al/Ga co-doped ZnO an up-shift of the Fermi-level by 0.6 eV and accordingly a decrease in resistivity caused by extrinsic doping has been reported.<sup>60</sup>

#### IV. CONCLUSIONS

We have successfully generated ZnO nanoparticles by using high-energy ball milling. Very pure samples were obtained for which the crystallite size could be adjusted by a careful choice of the milling time. This preparation route is facile and economically friendly, allowing for a significant reduction of the processing temperature in comparison to any other reported method for fabrication of nanocrystalline ZnO. Advanced characterisation techniques such as EPR, Raman, and impedance spectroscopy revealed detailed information on the electronic, vibrational, and electrical transport

properties. According to our experimental results, we introduced a *core-shell* model and determined the thickness of the *shell* as 0.5 nm. The origin of the observed non-linearity in the  $U$ - $I$  characteristics of nanocrystalline ZnO with particle sizes below 30 nm is consistent with this model.

#### ACKNOWLEDGMENTS

This research has been financially supported by the Deutsche Forschungsgemeinschaft, DFG (Grant: Er 662/1-1). S. K. S. Parashar is thankful to Indian Academy of Sciences, Bangalore, India, for support of Sciences Academies Summer Research Fellowship. The authors thank Prof. R. Böttcher from University of Leipzig and Dr. Ö. F. Erdem from MPI Mülheim for helpful discussions, Ms. A. Becherer (A.K. Hillebrecht, University of Freiburg) for performing Raman measurements, and Dipl. Phys. S. Gutsch (A.K. Zacharias, IMTEK, University of Freiburg) for SEM and EDX measurements.

- <sup>1</sup>G. Hodes, *Adv. Mater.* **19**, 639 (2007).
- <sup>2</sup>A. Janotti and C. G. Van de Walle, *Rep. Prog. Phys.* **72**, 126501 (2009).
- <sup>3</sup>U. Ozgur, Y. I. Alivov, C. Liu, A. Teke, M. A. Reshchikov, S. Dogan, V. Avrutin, S. J. Cho, and H. Morkoc, *J. Appl. Phys.* **98**, 041301 (2005).
- <sup>4</sup>F. A. Kröger, *The Chemistry of Imperfect Crystals* (North-Holland, Amsterdam, 1974).
- <sup>5</sup>S. Chawla, K. Jayanthi, and R. K. Kotnala, *Phys. Rev. B* **79**, 125204 (2009).
- <sup>6</sup>A. Paracchino, V. Laporte, K. Sivula, M. Gratzel, and E. Thimsen, *Nature Mater.* **10**, 456 (2011).
- <sup>7</sup>Y. Qin, X. Wang, and Z. L. Wang, *Nature* **451**, 809 (2008).
- <sup>8</sup>J. Zhou, P. Fei, Y. Gu, W. Mai, Y. Gao, R. Yang, G. Bao, and Z. L. Wang, *Nano Lett.* **8**, 3973 (2008).
- <sup>9</sup>S. T. Teklemichael, W. M. Hlaing Oo, M. D. McCluskey, E. D. Walter, and D. W. Hoyt, *Appl. Phys. Lett.* **98**, 232112 (2011).
- <sup>10</sup>K. Hoffmann and D. Hahn, *Phys. Status Solidi A* **24**, 637 (1974).
- <sup>11</sup>J. W. Allen, *Semicond. Sci. Technol.* **10**, 1049 (1995).
- <sup>12</sup>M. S. Kim, Y.-S. Kim, and C. H. Park, *Curr. Appl. Phys.* **11**, S288 (2011).
- <sup>13</sup>J. T. H. Tsai, B. H. B. Lee, and M. S. Yang, *Phys. Rev. B* **80**, 245215 (2009).
- <sup>14</sup>J. Zhou, Y. Gu, Y. Hu, W. Mai, P.-H. Yeh, G. Bao, A. K. Sood, D. L. Polla, and Z. L. Wang, *Appl. Phys. Lett.* **94**, 191103 (2009).
- <sup>15</sup>Y. Jin, J. Wang, B. Sun, J. C. Blakesley, and N. C. Greenham, *Nano Lett.* **8**, 1649 (2008).
- <sup>16</sup>C. Jagadish and S. J. Pearton, *Zinc Oxide Bulk, Thin Films and Nanostructures Processing, Properties, and Applications* (Elsevier, Hong Kong, 2006).
- <sup>17</sup>S. S. Kurbanov, G. N. Panin, T. W. Kim, and T. W. Kang, *Phys. Rev. B* **78**, 045311 (2008).
- <sup>18</sup>E. Erdem, P. Jakes, S. K. S. Parashar, K. Kiraz, M. Somer, A. Rüdiger, and R.-A. Eichel, *J. Phys.: Condens. Matter* **22**, 345901 (2010).
- <sup>19</sup>J. J. Schneider, R. C. Hoffmann, J. Engstler, A. Klyszcz, E. Erdem, P. Jakes, R.-A. Eichel, L. Pitta-Bauermann, and J. Bill, *Chem. Mater.* **22**, 2203 (2010).
- <sup>20</sup>J. J. Schneider, R. C. Hoffmann, J. Engstler, S. Dilfer, A. Klyszcz, E. Erdem, P. Jakes, and R.-A. Eichel, *J. Mater. Chem.* **19**, 1449 (2009).
- <sup>21</sup>M. C. Newton, S. J. Leake, R. Harder, and I. K. Robinson, *Nature Mater.* **9**, 120 (2010).
- <sup>22</sup>L. Dai, X. L. Chen, X. Zhang, T. Zhou, and B. Hu, *Appl. Phys. A* **78**, 557 (2004).
- <sup>23</sup>K. M. Sancier, *J. Phys. Chem.* **76**, 2527 (1972).
- <sup>24</sup>B. L. Yu, C. S. Zhu, F. X. Gan, and Y. B. Huang, *Mater. Lett.* **33**, 247 (1998).
- <sup>25</sup>Y. Hu and H. J. Chen, *J. Nanopart. Res.* **10**, 401 (2008).
- <sup>26</sup>A. Janotti and C. G. Van de Walle, *Appl. Phys. Lett.* **87**, 122102 (2005).
- <sup>27</sup>W. E. Carlos, E. R. Glaser, and D. C. Look, *Physica B* **308**, 976 (2001).
- <sup>28</sup>D. Galland and A. Herve, *Phys. Lett. A* **33**, 1 (1970).
- <sup>29</sup>C. Gonzalez, D. Block, R. T. Cox, and A. Herve, *J. Cryst. Growth* **59**, 357 (1982).

- <sup>30</sup>M. Kakazey, M. Vlasova, M. Dominguez-Patino, G. Dominguez-Patino, T. Sreckovic, and N. Nikolic, *Sci. Sinter.* **36**, 65 (2004).
- <sup>31</sup>N. G. Kakazey, T. V. Sreckovic, and M. M. Ristic, *J. Mater. Sci.* **32**, 4619 (1997).
- <sup>32</sup>S. Moribe, T. Ikoma, K. Akiyama, Q. W. Zhang, F. Saito, and S. Tero-Kubota, *Chem. Phys. Lett.* **436**, 373 (2007).
- <sup>33</sup>V. A. Nikitenko, *J. Appl. Spectrosc.* **57**, 367 (1992).
- <sup>34</sup>A. Pöpl and G. Völkel, *Phys. Status Solidi A* **121**, 195 (1990).
- <sup>35</sup>A. Pöpl and G. Völkel, *Phys. Status Solidi A* **125**, 571 (1991).
- <sup>36</sup>K. M. Whitaker, S. T. Ochsenein, V. Z. Polinger, and D. R. Gamelin, *J. Phys. Chem. C* **112**, 14331 (2008).
- <sup>37</sup>R. Laiho, L. S. Vlasenko, and M. P. Vlasenko, *J. Appl. Phys.* **103**, 123709 (2008).
- <sup>38</sup>N. G. Romanov, D. O. Tolmachev, A. G. Badalyan, R. A. Babunts, P. G. Baranov, and V. V. Dyakonov, *Physica B* **404**, 4783 (2009).
- <sup>39</sup>L. S. Vlasenko and G. D. Watkins, *Phys. Rev. B* **71**, 125210 (2005).
- <sup>40</sup>S. M. Evans, N. C. Giles, L. E. Halliburton, and L. A. Kappers, *J. Appl. Phys.* **103**, 043710 (2008).
- <sup>41</sup>N. Y. Garces, L. Wang, L. Bai, N. C. Giles, L. E. Halliburton, and G. Cantwell, *Appl. Phys. Lett.* **81**, 622 (2002).
- <sup>42</sup>K. Vanheusden, W. L. Warren, C. H. Seager, D. R. Tallant, J. A. Voigt, and B. E. Gnade, *J. Appl. Phys.* **79**, 7983 (1996).
- <sup>43</sup>D. C. Look, R. L. Jones, J. R. Sizelove, N. Y. Garces, N. C. Giles, and L. E. Halliburton, *Phys. Status Solidi A* **195**, 171 (2003).
- <sup>44</sup>V. Ischenko, S. Polarz, D. Grote, V. Stavarache, K. Fink, and M. Driess, *Adv. Funct. Mater.* **15**, 1945 (2005).
- <sup>45</sup>K. Leutwein and J. Schneider, *Z. Naturforsch., A: Phys. Sci.* **26**, 1236 (1971).
- <sup>46</sup>R. Laiho, D. S. Poloskin, Y. P. Stepanov, M. P. Vlasenko, L. S. Vlasenko, and V. S. Zakhvalinskii, *J. Appl. Phys.* **106**, 7 (2009).
- <sup>47</sup>A. Janotti and C. G. van de Walle, *Phys. Rev. B* **76**, 165202 (2007).
- <sup>48</sup>P. Lommens, K. Lambert, F. Loncke, D. De Muynck, T. Balkan, F. Vanhaecke, H. Vrielinck, F. Callens, and Z. Hens, *Chem. Phys. Chem.* **9**, 484 (2008).
- <sup>49</sup>L. Q. Jing, Z. L. Xu, J. Shang, X. J. Sun, W. M. Cai, and H. C. Guo, *Mater. Sci. Eng., A* **332**, 356 (2002).
- <sup>50</sup>A. L. Taylor, G. Filipovi, and G. Lindeber, *Solid State Commun.* **8**, 1359 (1970).
- <sup>51</sup>L. Y. Zhang, L. W. Yin, C. X. Wang, N. Lun, Y. X. Qi, and D. Xiang, *J. Phys. Chem. C* **114**, 9651 (2010).
- <sup>52</sup>P. Jakes and E. Erdem, *Phys. Status Solidi (RRL)* **5**, 56 (2011).
- <sup>53</sup>S. J. Jiao, Y. M. Lu, D. Z. Shen, Z. Z. Zhang, B. H. Li, Z. H. Zheng, B. Yao, J. Y. Zhang, D. X. Zhao, and X. W. Fan, *J. Lumin.* **122**, 368 (2007).
- <sup>54</sup>J. Nayak, S. Kimura, and S. Nozaki, *J. Lumin.* **129**, 12 (2009).
- <sup>55</sup>W. Lee, M. C. Jeong, M. J. Kim, and J. M. Myoung, *Phys. Lett. A* **370**, 345 (2007).
- <sup>56</sup>Y. Ueda, K. Yoshida, and H. Saitoh, *J. Ceram. Soc. Jpn.* **117**, 508 (2009).
- <sup>57</sup>P. R. Bueno, J. A. Varela, and E. Longo, *J. Eur. Ceram. Soc.* **28**, 505 (2008).
- <sup>58</sup>J. Jose and M. A. Khadar, *Mater. Sci. Eng., A* **304**, 810 (2001).
- <sup>59</sup>B. Wang, J. Min, Y. Zhao, W. Sang, and C. Wang, *Appl. Phys. Lett.* **94**, 192101 (2009).
- <sup>60</sup>W. Lee, S. Shin, D.-R. Jung, J. Kim, C. Nahm, T. Moon, and B. Park, *Curr. Appl. Phys.* **12**, 628 (2012).
- <sup>61</sup>See supplementary material at <http://dx.doi.org/10.1063/1.4725478> for this supplementary material includes supporting information about experimental and results section. In experimental supplementary we give some details about the high energy ball milling technique and the synthesis of ZnO nanocrystals. In this section we give also detailed description of the characterization methods that we used: TEM, SEM, XRD, EPR, Raman and Impedance. In the second part we give additional results which support the findings in the paper. XRD, SEM, TEM, EDX results give detailed information about the crystal structure whereas Raman, impedance and spin counting procedure give detailed information on the electronic structure.